

Use of terrestrial photosieving and airborne topographic LiDAR to assess bed grain size in large rivers: a study on the Rhine River

Valentin Chardon, Laurent Schmitt, Hervé Piégay, Dimitri Lague

▶ **To cite this version:**

Valentin Chardon, Laurent Schmitt, Hervé Piégay, Dimitri Lague. Use of terrestrial photosieving and airborne topographic LiDAR to assess bed grain size in large rivers: a study on the Rhine River. Earth Surface Processes and Landforms, 2020, 45 (10), pp.2314-2330. 10.1002/esp.4882 . hal-03004392

HAL Id: hal-03004392
https://hal.science/hal-03004392

Submitted on 26 Nov 2020

HAL is a multi-disciplinary open access archive for the deposit and dissemination of scientific research documents, whether they are published or not. The documents may come from teaching and research institutions in France or abroad, or from public or private research centers.

L'archive ouverte pluridisciplinaire **HAL**, est destinée au dépôt et à la diffusion de documents scientifiques de niveau recherche, publiés ou non, émanant des établissements d'enseignement et de recherche français ou étrangers, des laboratoires publics ou privés.

Use of terrestrial photosieving and airborne topographic LiDAR to assess bed grain size in large rivers: potentials and limits

Authors: Valentin Chardon[1,2], Laurent Schmitt[1], Hervé Piégay[2], Dimitri Lague[3]

1. CNRS UMR 7362 LIVE, University of Strasbourg, Strasbourg, France

2. CNRS UMR 5600 EVS, University of Lyon/Site ENS, Lyon, France

3. CNRS UMR 6118 GEOSCIENCES Rennes, University of Rennes 1, Rennes, France

Correspondence to: Valentin Chardon, CNRS UMR 7362 LIVE & 5600 UMR 5600, University of Strasbourg, 3 Rue de l'Argonne 67000 Strasbourg Cedex. E-mail: valentin.chardon@live-cnrs.unistra.fr. Telephone number: +33 3 68 85 09 76

Abstract (300 mots-max)

Most grain size monitoring is still being conducted by manual sampling in the field, which is time consuming and has low spatial representation. Due to new remote sensing methods, some limitations have been partly overcome, but methodological progress is still needed for large rivers as well as in underwater conditions. In this paper, we tested the reliability of two methods along the Old Rhine River (France/Germany) to estimate the grain size distribution (GSD) in above-water conditions: (i) a low-cost terrestrial photosieving method based on an automatic procedure using Digital Grain Size (DGS) software and (ii) an airborne LiDAR topo-bathymetric survey. We also tested the ability of terrestrial photosieving to estimate the GSD in underwater conditions. Field pebble counts were performed to compare and calibrate both methods. The results showed that the automatic procedure of

terrestrial photosieving is a reliable method to estimate the GSD of sediment patches in both above-water and underwater conditions with clean substrates. Sensitivity analyses showed that environmental conditions, including solar lighting conditions and petrographic variability, significantly influence the GSD from the automatic procedure in above-water conditions. The presence of biofilm in underwater conditions significantly altered the GSD estimation using the automatic procedure, but the proposed manual procedure overcame this problem. The airborne LiDAR topographic survey is an accurate method to estimate the GSD of above-water bedforms and is able to generate grain size maps. The combination of terrestrial photosieving and airborne topographic LiDAR methods is adapted to assess the GSD along large rivers in entire sections that are several kilometers long.

Key words: Grain size, Large rivers, above-water and underwater conditions, Methodological study, Terrestrial photosieving, Airborne topographic LiDAR.

1. Introduction

Quantification of the GSD of a riverbed surface is important for assessing sediment transport and for geomorphological and ecological studies, notably regarding river restoration (Graham, Rice, and Reid, 2005b; MacKenzie, Eaton, and Church, 2018). Many studies have been carried out during recent decades to characterize the GSD, but its assessment remains difficult because the grain size variability depends notably on the study scale (Church, Mclean, & Wolcott J.F, 1987; Graham et al., 2005b). GSD assessment of a sediment patch requires a large set of particles whose number depends on the shape of the distribution (Rice & Church, 1996). Most grain size monitoring was performed by using the classic “pebble count” manual procedure (Wolman, 1954). These different procedures are all time consuming and show low spatial representation, especially for large rivers (Warrick et al. 2009).

From the beginning of the 1970s, terrestrial photosieving methods were carried out to estimate the GSD in above-water conditions to reduce field time, increase the sampling density and limit bed disturbance (Butler, Lane, and Chandler 2001). Data processing requires manually digitizing the B-axis of each visible particle, increasing the time and lab effort (Kellerhals & Bray, 1971; Ibbeken & Schleyer, 1986). Thereafter, semiautomatic or automatic procedures were developed to reduce the processing time. They were based either on oriented-object approaches (McEwan et al., 2000; Sime & Ferguson, 2003; Graham, Reid, and Rice, 2005a; Lucas & Strom, 1987; Detert & Weitbrecht, 2012; Strom, Kuhns, & Lucas, 2010; Sulaiman et al., 2014) or on statistical approaches (Buscombe, 2010, Buscombe, 2013; Sime & Ferguson, 2003; Warrick et al., 2009). However, this kind of method is suitable only for studies where prompt GSD data are needed.

Over the last two decades, new methods of remote sensing have been developed to estimate the GSD at larger spatial scales in above-water conditions (Dugdale, Carbonneau & Campbell, 2010). Some studies tested the reliability of airborne digital imagery processing, such as airborne multispectral (Rainey et al., 2003; Black et al., 2014) or color photography, by performing textural analyses to estimate the GSD over scales from several hundred meters to several dozen kilometers **(Carbonneau, Lane, & Bergeron, 2004; Carbonneau, Bergeron, & Lane, 2005; Verdú, Batalla, & Martínez-Casasnovas, 2005; Lejot et al., 2011; Carbonnneau, Bizzi, & Marchetti, 2018; Woodget, Fyffe, & Carbonneau, 2018).** The accuracy of these methods to predict the GSD is dependent on the resolution of the images, which must be commensurate with the particle size (Lejot et al., 2011). Three-dimensional data acquired by terrestrial LiDAR or UAV photogrammetry were also used to predict the GSD by using the bed surface roughness as a proxy (Heritage & Milan, 2009;

Brasington, Vericat, & Rychkov, 2012; Storz-Peretz & Laronne, 2013; Woodget & Austrums, 2017; Vázquez-Tarrío et al., 2017). The first empirical relation between the roughness height metric (rh) and the median grain size was found by Gomez (1993) from the bed surface profile and vertical photographs. These methods have the advantage that they simultaneously provide various information, such as roughness maps, channel morphological dynamics, and grain size maps (Marteau et al., 2017; Vázquez-Tarrío et al., 2017). However, the application of terrestrial LiDAR and UAV photogrammetry techniques is not applicable in large study reaches in underwater conditions.

During the last decade, airborne topographic LiDAR techniques have been increasingly employed, notably in fluvial geomorphological and hydrologic studies (Charlton, Large, & Fuller, 2003; Demarchi, Bizzi, & Piégay, 2016; Bizzi et al., 2019; Shaker, Yan, & LaRocque, 2019). Dataset collection is performed by using the near-infrared wavelength (Mandlburger et al., 2015). The data collection is fast and may cover large areas. This method provides not only accurate point clouds in three dimensions but also intensity values that correspond to the amplitude of the return signal (Kashani et al., 2015). Kukko, Kaasalainen, & Litkey, (2008) showed that this metric is impacted partly by surface roughness, suggesting a probable link between the intensity values and the bed grain size.

Some studies have been carried out to qualitatively estimate the GSD in underwater conditions, but they are rare due to technical limitations in constraining field conditions.

Qualitative underwater substrate mapping was produced by using side-scan sonar imagery (Buscombe, Grams, & Kaplinski, 2017, Buscombe, Grams, & Smith, 2015; Hamill, Buscombe, & Wheaton, 2018). Rüther (2013) used the terrestrial

photosieving method in underwater conditions along the Surna River to estimate the bed GSD following an automatic procedure but without a control dataset and calibration with field GSD.

This paper addresses the inference of the GSD in large rivers from remote sensing in both above-water and underwater conditions. Two methods are tested in above-water conditions: (i) terrestrial photosieving, a low-cost technique to rapidly estimate the bed GSD, and (ii) airborne topographic LiDAR data analysis using a laser wavelength λ=1064 nm. For underwater conditions, we tested the terrestrial photosieving method. This paper follows three objectives: (i) compare the reliability between the terrestrial photosieving technique and the airborne LiDAR topometric survey in above-water conditions, (ii) test the reliability of the terrestrial photosieving technique to estimate the GSD in underwater conditions and (iii) determine the parameters that can influence the accuracy of both techniques in both environmental conditions.

2. Materials and methods

2.1 Study area

The Rhine is the third largest river in Europe with a drainage basin of approximately 185,000 km² and a length of 1250 km. The Upper Rhine runs from Basel to Bingen-am-Rhein (300 km long) into the Upper Rhine graben, where the hydrological regime is nivo-glacial (Figure 1.a). The mean annual discharge is 1059 m^3/s at Basel (Uehlinger & Wantzen, 2009). After two engineering phases of correcting and regulating the flow (Arnaud, 2012; Schmitt, Morris, & Kondolf, 2018), the Old Rhine River was bypassed by the French Grand Canal d'Alsace (GCA) along 50 km from Kembs to Breisach. Most of the flow of the Rhine River into the GCA is regulated by the Kembs derivation dam. The GCA has four power plants. An instream flow is maintained in the Old Rhine between 52 and 115 m^3/s, which is the monthly variation corresponding to the natural hydrological discharge of the Rhine River (Figure 1.b). Spillovers occur into the Old Rhine River when the Rhine discharge exceeds 1400 m^3/s at Basel, which corresponds to the maximum discharge of the GCA capacity. The channel bottom of the Old Rhine River is composed of gravels to cobbles. The mean slope and mean width are equal to 0.09% and 100 m, respectively (Figure 1.b).

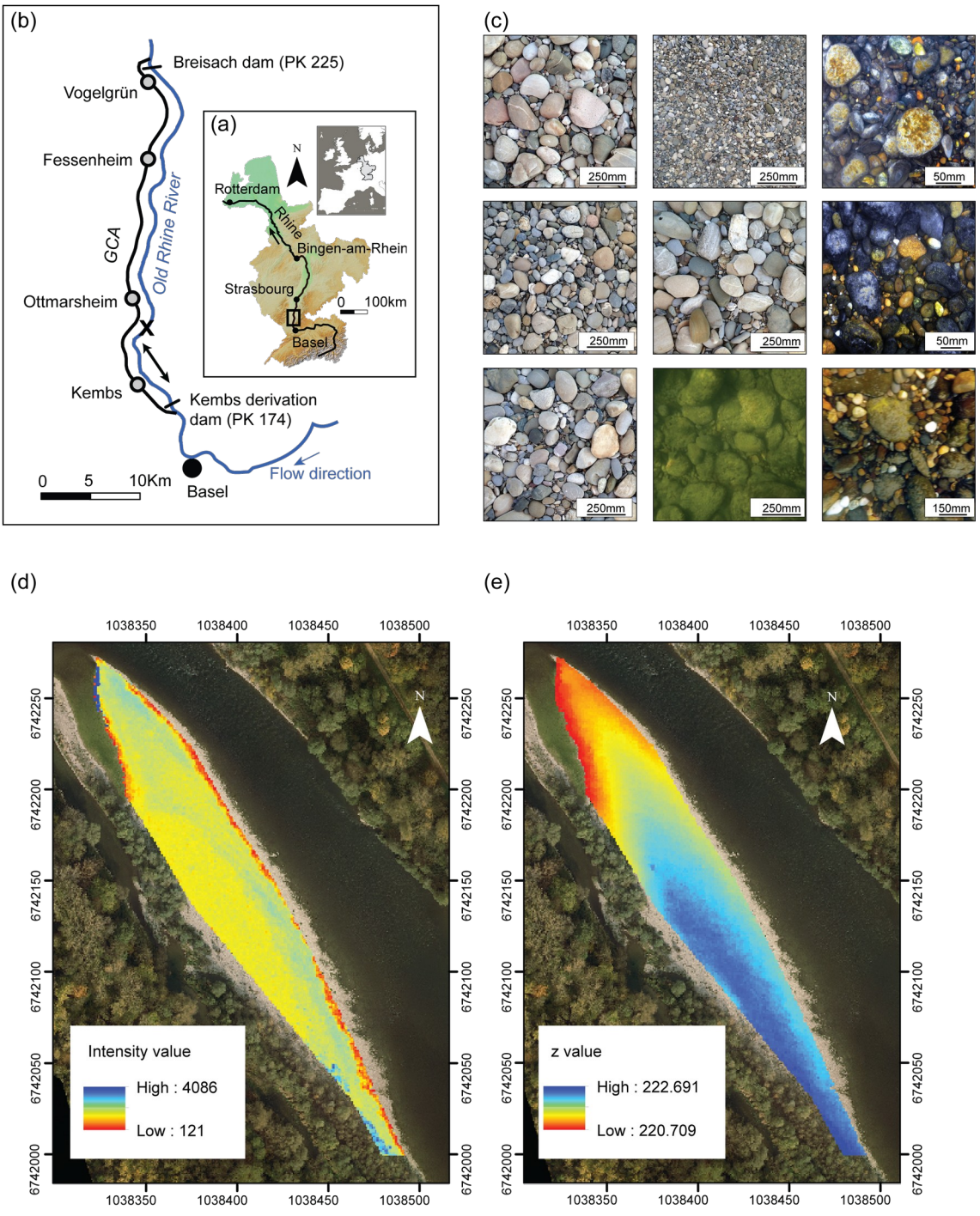


Figure 1: (a) The Rhine Basin and the location of the study reach, (b) the Old Rhine River and the GCA, (c) the range of digital images collected in this study, and (d) and (e) maps of the intensity values and the Rh roughness metric of an above-water deposit along the study reach. In (a), the black rectangle indicates the location of the Old Rhine River. In (b), the black arrows, the black cross and the gray circles

represent the study reach, the Rheinweiler gauging station and the power plants, respectively.

2.2 Data collection

2.2.1 Collection of digital images

Between winter and autumn 2017, terrestrial photosieving surveys were carried out on both above-water and underwater patches by using a 12-MP Olympus TG-4 waterproof camera. The camera was placed in a plan view by using a telescopic rod. The recorded elevation ranged from 0.6 m to 1.0 m, and the pixel size ranged from 0.18 mm to 0.30 mm in above-water conditions and from 0.24 mm to 0.40 mm in underwater conditions. A square gabarit with an area of 1 m² placed on the bed surface and a rigid rule were used for scale in above-water and underwater conditions, respectively. All the digital images recorded in above-water conditions were characterized as clean substrate (n=10), while the digital images collected in underwater conditions were composed of both clean substrate (n=4) and substrate with biofilm (n=6).

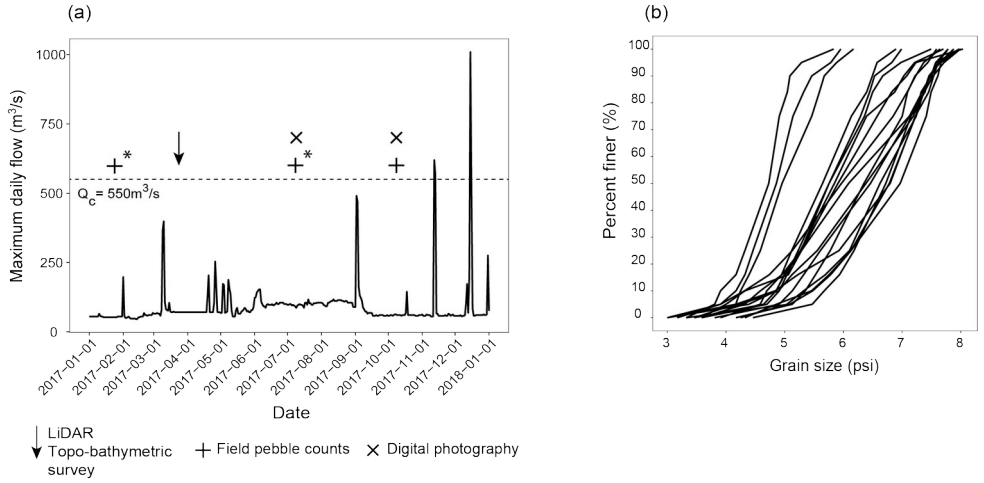


Figure 2. (a) Framework of the study and maximum daily flow at the Rheinweiler gauging station during 2017 and (b) the GSD of the field pebble counts (truncated at 3 psi). * indicates the collection period of the field pebble counts used for the

calibration of the airborne topo-bathymetric LiDAR survey. The value of the critical discharge was extracted from (El Kadi Abderrezzak, 2009).

2.2.2 Airborne topographic LiDAR survey

In March 2017, airborne LiDAR data were acquired by using a Teledyne Optech Titan DW sensor. The flight was carried out at an altitude of 400 m along a reach of 35 km between KP 174,00 and KP 209.00. The Titan DW sensor is a topo-bathymetric sensor operating a near-infrared (NIR) laser (λ=1064 nm) typical of airborne topographic LiDAR and a green laser (λ=532 nm) with shallow-water bathymetry mapping capability (Fernandez-Diaz et al. 2016) In this study, only the NIR laser data were used on above-water bars.

The divergence angle of the NIR laser is 0.3 mrad, resulting in a laser spot size of approximately 0.12 m at nadir. The range density points and range mean distance between points, 38 to 49 points/m^2 and 0.08 m to 0.09 m, respectively, were calculated on three-point clouds located on three above-water deposits. To estimate the range noise of the flight, we estimated the variability of the z-values and intensity values on three ground control areas (sections of roads) by assuming that the difference in the point values should be equal to 0 on planar control areas (Lague, Brodu, & Leroux, 2013). The uncertainties of the survey along the z-axis were less than 2 cm and equal to 2.10 cm for the intensity values (Table 1).

195

196

Standard deviation of z values deviation (cm)	Standard deviation of Rh metric deviation (cm)	Standard deviation of intensity values deviation	Standard deviation of intensity metric deviation
1.00	0.18	2.10	6.51
2.00	0.17	1.90	3.65
0.90	0.15	2.10	1.50

197 Table 1: Precision of the LiDAR topographic survey along three ground control areas.
198 LiDAR metrics were computed for a kernel size equal to 0.4 m.

199 2.2.3 Collection of field pebble counts

200 The collection of field pebble counts was based on the random surface sampling of
201 100 particles for each sediment patch during February 2017 and October 2017
202 (Wolman, 1954). A sampling of 21 pebble counts was collected in both above-water
203 (n=18) and underwater conditions (n=3) in a large range of sediment patches (Figure
204 2). The low number of field samplings in underwater conditions resulted from adverse
205 survey conditions due to bed imbrication, high water depth and flow velocity and the
206 locally important thickness of fine sediments (greater than 0.1 m). On above-water
207 surfaces, each particle was collected at every 2*Dmax (Dmax=maximum B-Axis)
208 spacing along a decameter. In underwater conditions, the particles were sampled
209 following the random step-toe procedure (Bunte & Abt, 2001). A caliper was used to
210 measure the B-axis of each particle. The distribution was truncated at 3 psi according
211 to the results of Rice & Church, (1996), who demonstrated an underestimation for
212 these particles during pebble count sampling. Each pebble count area was
213 georeferenced by using a global positioning system (centimetric planimetric
214 precision). For calibration purposes, ten field pebble counts in above-water

conditions and three field pebble counts in underwater conditions were compared to the terrestrial photosieving results. On the other hand, 18 field pebble counts were used to calibrate the LiDAR metrics. The ranges of the 50^{th} and 84^{th} percentiles of the sampled sediment patches were between 4.75 psi and 7.02 psi and between 5.04 psi and 7.49 psi, respectively.

2.3 Data processing

2.3.1 Automated processing of digital images

Digital Grain Size (DGS) software developed by Buscombe (2013) was used to automatically estimate the GSD of the apparent particle B-axis. This software, which is based on the wavelet statistical approach, provided the distribution in grid by number form. From the recommendations of Barnard et al., (2007) and Buscombe (2010), a control dataset composed of twenty digital images was used to evaluate the accuracy of the software. The control dataset was performed by using the grid tool implemented in ImageJ software.

2.3.2 Manual processing of digital images

A manual method was also tested to process the digital images to compare with the automatic procedure. The B-axis of particles was manually digitalized following a grid in which nodes were spaced by one Dmax to avoid sampling the same particle twice. This was made by the same operator to minimize the subjective bias during the B-axis choice. This procedure was performed by using the grid tool implemented on ImageJ software. Sampling areas were equal to 100 times the area of the largest particle following Petrie & Diplas (2000) recommendation.

2.3.3 Processing the airborne topographic LiDAR survey

2.3.3.1 Computation of the Rh metric

First, all vegetation areas were excluded from the point cloud to avoid computation errors by empirically filtering the intensity values because it can be a more accurate method than geometric classification approaches (Reymann & Lacroix, 2015). The Rh metric was computed by using the roughness tool implemented in CloudCompare v.2.9.1 software (EDF R&D). For each point, the computation of the Rh metric is given by the distance between the point elevation and the ordinary least-squares best fitting plane computed on its nearest neighbors (Woodget, 2015; Woodget et al., 2017; Vázquez-Tarrío et al., 2017). The nearest neighbors are selected within a specified kernel size from the selected point. Third, according to the methodology of Vázquez-Tarrío et al., (2017), the point cloud was clipped by a buffer with a radius of five meters, and the center corresponded to the location of the field pebble counts to compare the Rh metric distribution with the field GSD. This step was performed by using ArcGIS software.

2.3.3.2 Computation of the standard deviation of the intensity values

The intensity values of the return pulses of the NIR wavelength are influenced by several parameters, including internal instrument amplification, environmental effects (wetness and atmospheric transmittance), data acquisition geometry (range and incidence angle) and surface characteristics (reflectance and roughness) (Li et al., 2014; Kashani et al., 2015). In our case study, instrumental and environmental parameters had a limited impact on intensity values because the same instrument was used, and environmental conditions, including the flight elevation, were relatively constant during flight. Considering the data acquisition geometry, Kukko, Kaasalainen, & Litkey (2008) and Kaasalainen et al., (2011) showed that intensity

values are significantly sensitive to the incidence angle when the latter is greater than 20°. In our case, the incidence angle did not exceed 16°, and we assumed that the data acquisition geometry had no influence. Hence, we tested the standard deviation of the raw values of intensity as a proxy for the surface GSD. The first step consisted of calculating the standard deviation of the raw intensity values for each point of the point cloud for a given area by computing a buffer with a specific radius. We performed this step by using ArcGIS software. The second step was identical to the third step of the computation of the Rh metric (see section 2.3.4).

2.4 Sensitivity analyses

2.4.1 Effect of environmental conditions on GSD estimation by the DGS software

Sensitivity analyses were performed on three parameters:

1. The influence of the textural variation of the digital image induced by petrographic variability. This study was performed by using a median filter that homogenized the textural differences within individual particles and reduced the oversegmentation (Strom, Kuhns, & Lucas, 2010). The kernel size of the median filter was increased progressively to 1%, 2.5%, and 5% for underwater conditions (n=6) and increased progressively to 1%, 2.5%, 5%, 10% and 15% of the maximal B-axis of the largest particle observed on each digital image for above-water conditions with controlled solar lighting conditions (n=10). The GSDs estimated by the software were compared to the control dataset.
2. The light conditions during digital image acquisition. We recorded two photographs for each sampling patch (n=10) with and without sun exposure by using an umbrella on the above-water clean substrate. The time recording was extracted from the raw data digital image to calculate the influence of the solar angle on the GSD estimation.

3. The quality of the substrate on the DGS error estimations as clean substrate or substrate with the presence of biofilm.

2.4.2 Selection of minimal sampling area in the DGS software

To evaluate the effect of the minimal sampling area on the estimation fluctuations of the DGS software, for each sediment patch in above-water conditions (n=10), we increased the minimal sampling area progressively from 10 to 100 times the area of the largest particle by steps of 10 by using a montage of digital images performed with GIMP software. We calculated a mobile slope coefficient to determine from which sampling area the fluctuation estimations were low as follows:

$Slope\,coefficient = ¿¿$

2.4.3 Airborne topographic LiDAR

The accuracy of the GSD predicted by the Rh metric can be influenced by the kernel size computation of the metric (Vázquez-Tarrío et al., 2017; Woodget & Austrums, 2017). A sensitivity analysis was performed by computing the Rh metric for kernel sizes ranging between 0.4 m and 2.0 m, by steps of 0.1 m from 0.4 m to 1.0 m, and by steps of 0.2 m from 1.0 m to 2.0 m. This procedure was performed using CloudCompare v.2.9.1 software. The same procedure was performed for the standard deviation of the intensity values using ArcMap v10.3 software by progressively increasing the size of the radius of the computed buffer.

We computed linear regressions between the two proxies with the field GSD for each kernel size to define the best relationship between the two variables and consequently to identify the best kernel size.

3. Results

3.1 Accuracy of the GSD estimation in above-water conditions using terrestrial photosieving

3.1.1 Accuracy of the DGS software

Figure 3 shows that the percentiles estimated by the DGS software in clean above-water conditions with clean substrate and controlled solar lighting conditions were systematically underestimated compared with the percentile values of the control dataset. For the 50th percentile, the values of the NRMSE were equal to 72% for the digital images with clean substrate in above-water conditions (Table 2). Error estimations decrease as the percentiles increase for these two types of ground digital images. The NRMSE values were 88% and 32% for the 5th percentile and the 95th percentile, respectively.

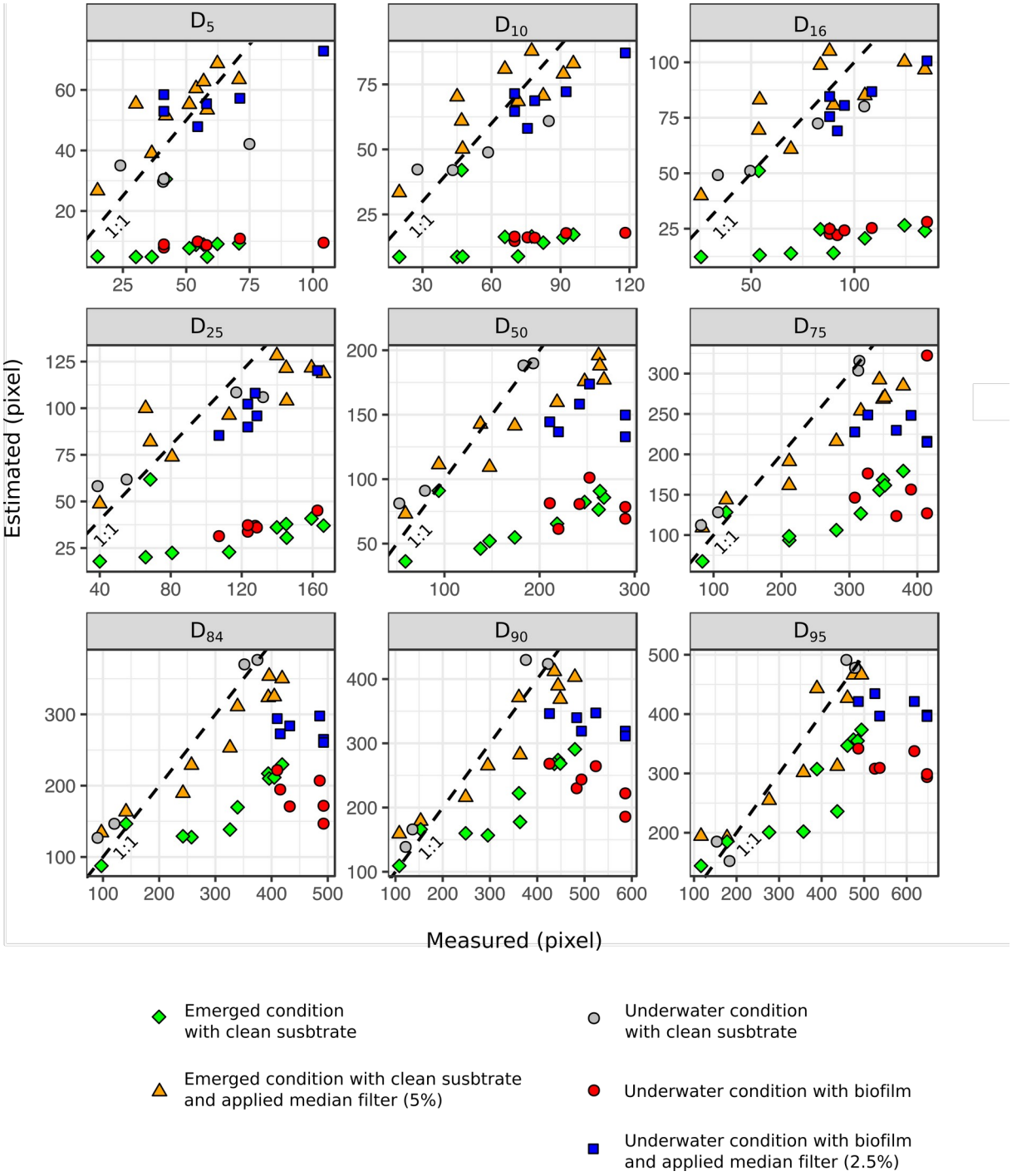


Figure 3: Estimated percentiles by the DGS software as a function of the percentile values of the control dataset. The dashed lines correspond to the 1:1 line. The digital images were taken with controlled solar lighting conditions in above-water conditions.

	Above-water condition		Underwater condition		
Decile	Clean substrate with	Clean substrate with	Clean substrate	Biofilm	Biofilm with median

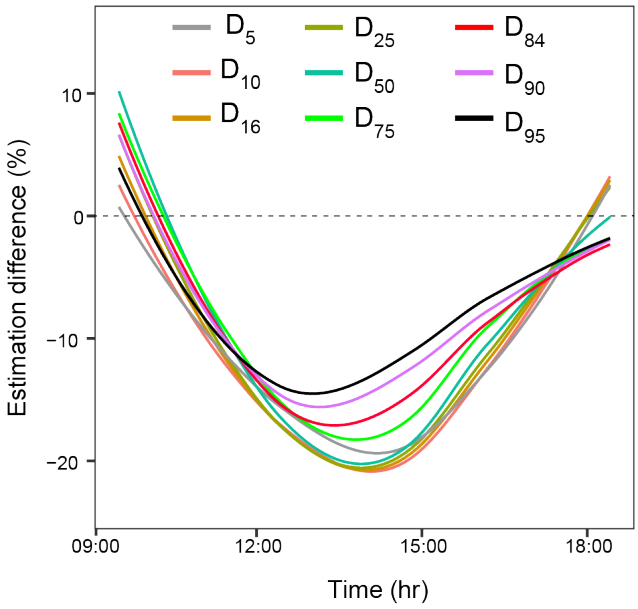
	controlled solar lighting condition (n=10)	median filter (5%) (n=10)	(n=4)	(n=6)	filter (2.5%) (n=6)
D_5	88	22	42	92	27
D_{10}	84	21	28	83	21
D_{16}	83	25	23	77	20
D_{25}	80	25	20	72	23
D_{50}	72	29	12	70	45
D_{75}	58	23	9	56	40
D_{84}	51	18	10	60	40
D_{90}	43	16	12	56	39
D_{95}	32	15	8	47	31

Table 2*:* Values of the normalized root mean square error (NRMSE) in percentage for each type of data. The RMSE values were normalized by the mean particle size of the corresponding percentile of the control dataset and multiplied by 100.

3.1.2 Effects of environmental conditions

3.1.2.1 Effects of solar lighting conditions

Figure 4 compares the percentiles estimated by the DGS software for the same digital image in sunny and shadow conditions. An overprediction below 10% was observed before 10:00 am for sunny conditions by comparison with shadow conditions. In contrast, underprediction was observed in sunny conditions with a peak of 20% for 2:00 pm. In any light condition, coarse percentiles are less impacted than small percentiles.



337

338 Figure 4: Impact of the solar lighting conditions on the GSD estimated by DGS
339 software.

340 3.1.2.2 Effects of the particle petrography

341 Figure 5.a-c shows the influence of the application of a median filter on a digital
342 image recorded in above-water conditions for a clean substrate. The filter produced
343 both a smoothing and a reduction in intravariability of the gray values of the pixels
344 that composed the particles, thus limiting intra-particle noise (Figure 5.b). Applying
345 the median filter reduced the NRMSE value of the estimated percentiles by the DGS
346 software up to a certain threshold. Figure 6.a shows that 5% of the B-axis of the
347 largest particle was the best compromise to minimize the estimated errors for all
348 percentiles. The application of this filter on the raw-clean substrate reduced the
349 estimated error percentiles by twice to four times (Table 2) and significantly reduced
350 the over-segmentation by the software (Figure 3). The NRMSE values decreased
351 from 83% to 25%, from 72% to 29% and from 51% to 18% for the 16th, 50th and 84th
352 percentiles, respectively.

The use of a median filter increased the data processing time. As shown in Figure 6.b, the computation of the median filter increased with increasing kernel size following a power function. For example, the computation time of a digital image with a size equal to 2748*2808 pixels was processed from 7 to 95 seconds for a kernel size equal to 1% and 5% of the B-axis of the largest particle.

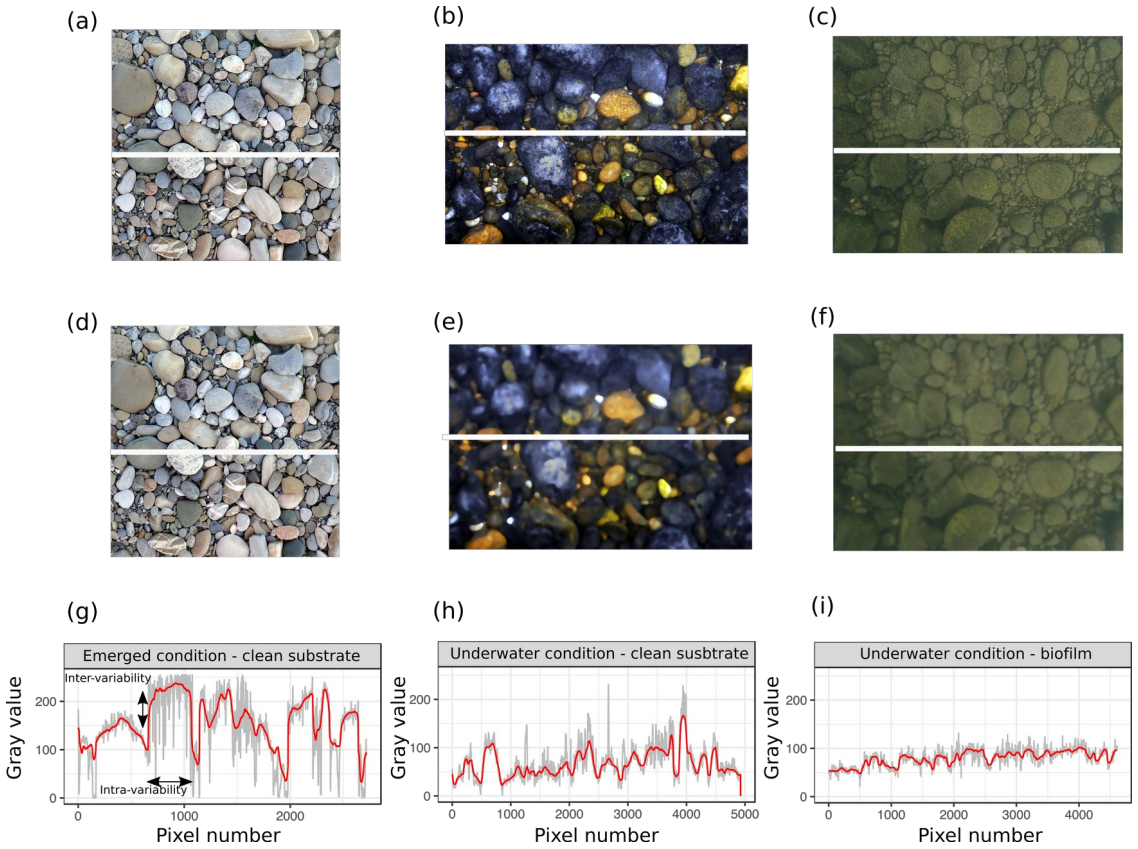


Figure 5: Effect of applying a median filter on gray values of digital images in different conditions: (a) and (d) correspond to a digital image of clean substrate in controlled solar lighting conditions in above-water conditions with and without the application of a median filter, respectively; (b) and (e) correspond to a digital image of clean substrate in underwater conditions with and without the application of a median filter, respectively; (c) and (f) correspond to a digital image of substrate with the presence of biofilm in underwater conditions with and without the application of a median filter, respectively. The gray line in (g), (h) and (i) corresponds to the gray values of pixels

extracted from the raw image, and the red line corresponds to the gray values of pixels extracted after the application of the median filter.

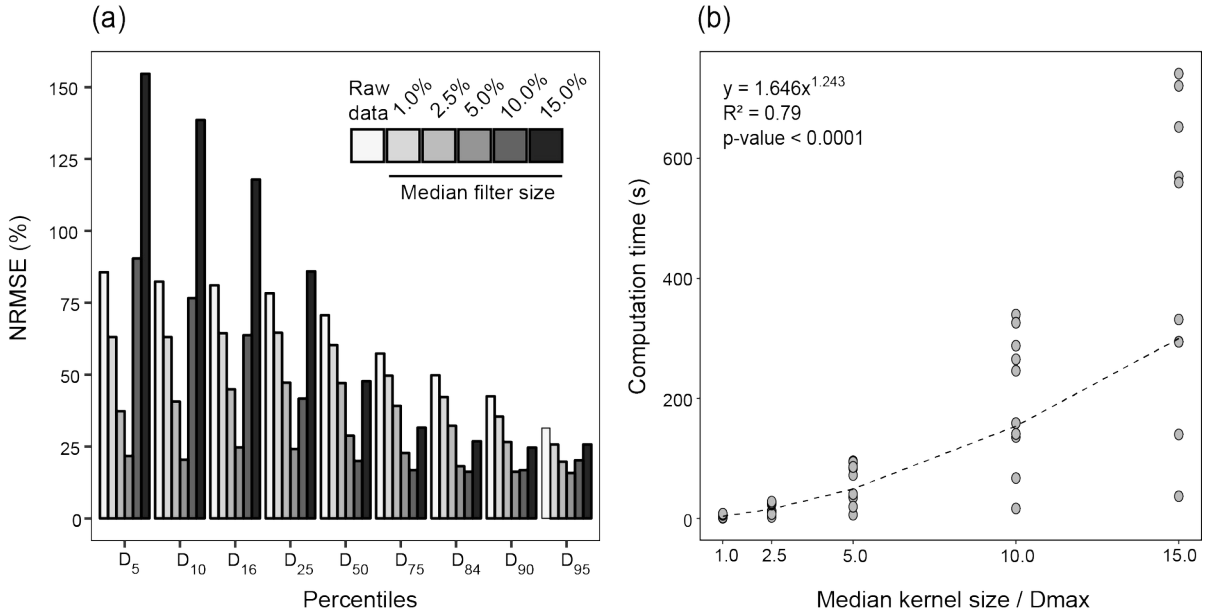


Figure 6: (a) Effect of applying the median filter to the model deviation for each percentile as a function of the kernel size. Percentage values correspond to the kernel size of the median filter divided by the B-axis of the largest particle, multiplied by 100.

3.1.3 Effect of sampling area

For all percentiles, a significant negative exponential relationship (95% confidence level) was found between the slope coefficient and the dimensionless sampling area (sampling area divided by the largest particle area; Figure 7.a). A stabilization of the values of the slope coefficient was observed from a sampling area equal to 80 times the area of the largest particle (Figure 7.b). The mean values of the slope decreased from 2.41 to 0.17 for dimensionless sampling areas from 20 to 80. It has been observed that the slope coefficients were higher for the sediment patches characterized by a high sediment sorting index than for sediment patches with low sediment sorting for the same sampling area (Figure 7.a).

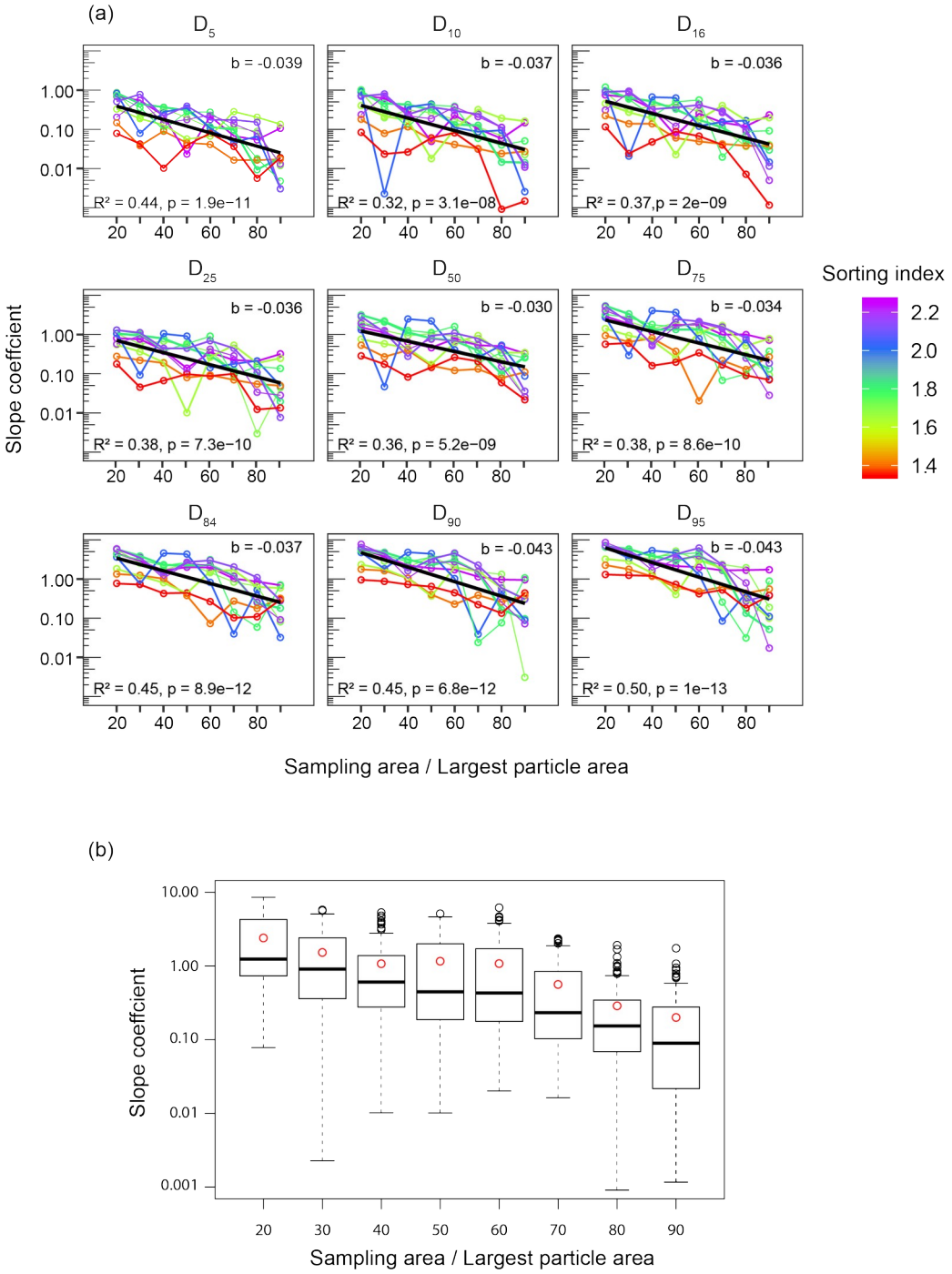


Figure 7: (a) Evolution of the slope coefficient as a function of the dimensionless sampling area and the sorting index, where black lines correspond to the relationship, and (b) boxplots of the slope values according to the dimensionless sampling area. Intervals correspond to the 25th and 75th percentiles, and the lower and upper whiskers correspond to 1.5 times the interval quartile range. Black lines correspond to the median values, and the red points correspond to the mean values.

3.1.4 Comparison of the estimated GSD with field pebble counts

Figure 8.a compares the percentiles estimated by field pebble counts with the percentiles estimated by the automatic procedure of the digital images in controlled environmental conditions (controlled solar lighting condition, application of the median filter at 5%, and sampling area greater than 80 times the largest particle). The terrestrial photosieving method quasi-systematically underestimated the field pebble-count percentiles. The bias of the terrestrial photosieving method has been corrected by linear regression (Figure 8.b). The RMSE values decreased from 0.55 psi to 0.29 psi by applying the correction. The comparison of our results with other studies using automatic procedures shows the same range of errors (Table 3).

Study	Approach	Form distribution	Lighting conditions	Range of grain size (psi)	Truncations	Irreducible error (e) (psi)
This study	Statistical approach	Pebble counts	Controlled	3.00 – 8.13	3 psi	0.29
This study	Manual approach	Pebble counts	Not controlled	3.00 – 8.13	3 psi	0.29
Sime & Ferguson, (2003)	Object-oriented approach	Pebble counts	Not specified	Not specified	3 psi	0.27
Graham et al., (2005.b)	Object-oriented approach	Pebble counts	Controlled	0.10 – 7.64	3 psi	0.18 [(a)]
Strom et al., (2010)	Object-oriented approach	Pebble counts	Not specified	2.32 – 7.60	2.32 psi	0.26

Table 3: Comparison of the performance of the procedures used in this study with those used in other published studies. All values are in psi. The irreducible error (e) of Graham et al. (2005b) was transformed to grid by number distribution. [(a)] Mean irreducible error calculated on three rivers.

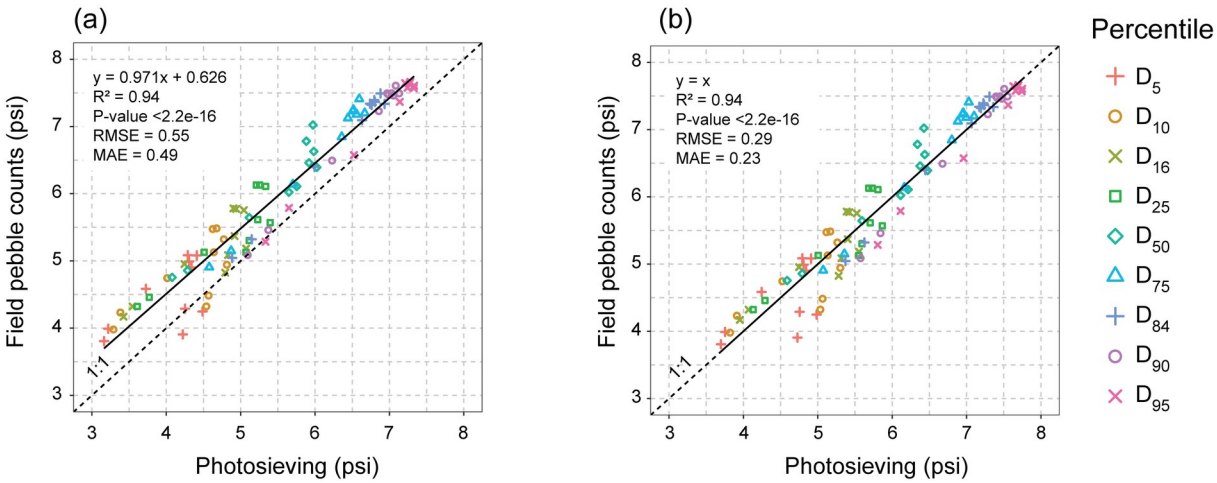


Figure 8: Percentiles estimated by field pebble counts according to percentiles estimated by the automatic procedure of digital images (a) before the bias correction and (b) after the bias correction. RMSE and MAE values are in psi. The distributions were truncated at 3 psi.

3.2 Accuracy of the GSD estimation in above-water conditions by using airborne topographic LiDAR data

3.2.1 Rh metric and standard deviation of intensity values as proxies of the GSD

The percentiles calculated using the distribution of the standard deviation of the intensity values were higher than the threshold uncertainties for all percentiles (Figure 9.a). For the Rh metric, only the percentiles equal to or greater than the 25th were greater than the threshold uncertainties.

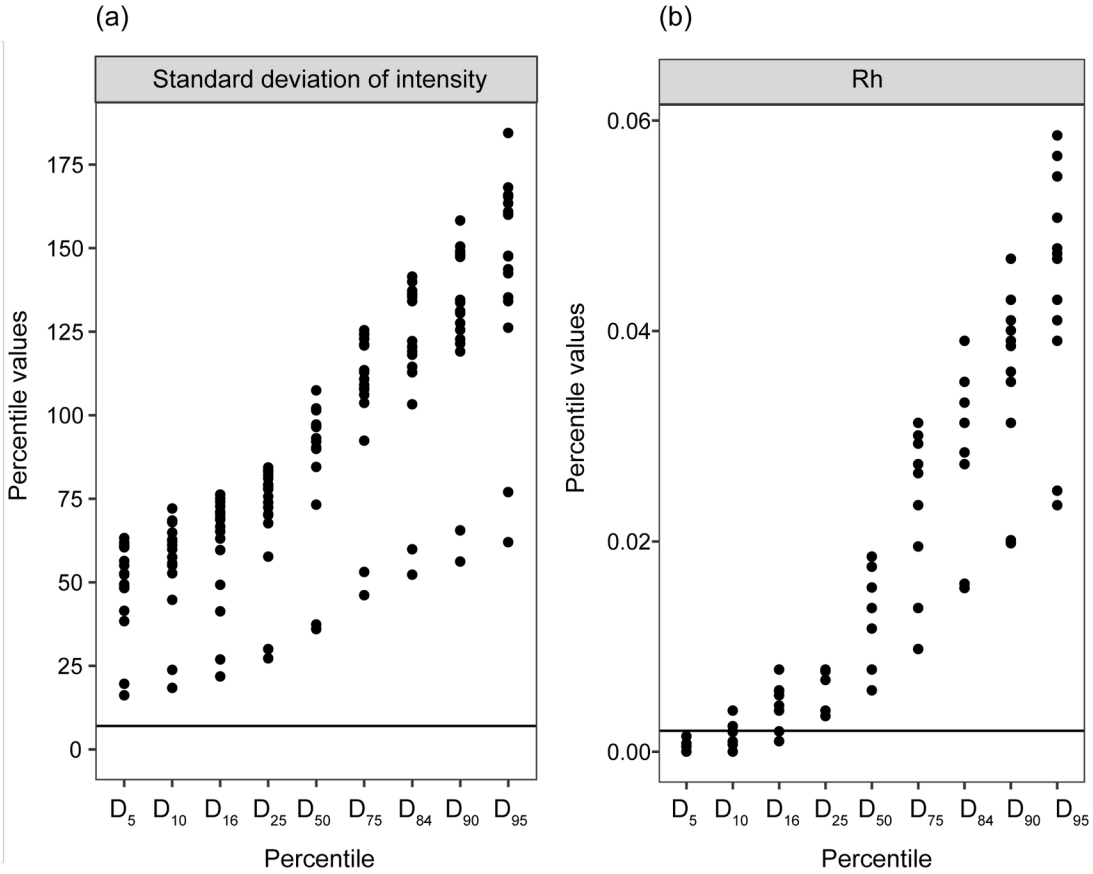


Figure 9: Values of percentiles estimated by (a) the standard deviation of the intensity values and (b) the Rh metric extracted from the airborne topographic LiDAR survey. The black line corresponds to the threshold uncertainties of the two metrics estimated on the three control areas (see section 2.2.2).

Significant power law correlations at the 95% confidence level were found between the percentiles of the Rh metric distribution and the GSD of the field pebble counts in a range of grain sizes equal to or higher than the 25th percentile (Table 4). The strongest correlation was found for the 84th percentile with an R^2 coefficient equal to 0.85 (p-value=4.9e-08). Significant power law correlations at the 95% confidence level were also found between the percentiles of the distribution of the standard deviation of the intensity values and the GSD of the field pebble counts (Table 4). The strongest correlation is also found for the 84th percentile with an R^2 coefficient equal to 0.85 (p-value=9.6e-07) (Table 4). Figure 10.a-b shows that the relationship

between the predicted percentiles by both metrics and the estimated percentiles by the field pebble counts are close to the 1:1 line. The mean values of the RMSE and MAE of the predicted GSD were equal to 0.34 psi and 0.29 psi for the Rh metric for the 16^{th} and 95^{th} percentile, respectively, while for the standard deviation of the intensity values, the mean values of the RMSE and MAE were equal to 0.38 psi and 0.30 psi for the 5^{th} and 95^{th} percentile, respectively (Figure 10.a-b).

	Rh metric (n=18)					Standard deviation of intensity values (n=18)				
Percentile	Equation	R^2	p-value	RMSE	MAE	Equation	R^2	p-value	RMSE	MAE
D_5	NE	NE	NE	NE	NE	$y=2.528x^{0.154}$	0.32	0.013	0.40	0.31
D_{10}	NE	NE	NE	NE	NE	$y=2.41x^{0.180}$	0.41	0.0048	0.39	0.31
D_{16}	NE	NE	NE	NE	NE	$y=12.138x^{0.219}$	0.61	0.00035	0.32	0.28
D_{25}	$y=30.280x^{0.345}$	0.62	9.4e-05	0.36	0.30	$y=1.800x^{0.264}$	0.67	0.00015	0.34	0.30
D_{50}	$y=23.994x^{0.319}$	0.69	2.2e-05	0.38	0.31	$y=1.450x^{0.318}$	0.78	3.2e-05	0.32	0.26
D_{75}	$y=23.654x^{0.341}$	0.79	8.8e-07	0.34	0.28	$y=1.110x^{0.387}$	0.82	2.2e-06	0.33	0.25
D_{84}	$y=29.015x^{0.410}$	0.85	4.9e-08	0.29	0.26	$y=1.103x^{0.386}$	0.85	9.6e-07	0.31	0.24
D_{90}	$y=28.590x^{0.422}$	0.81	3.5e-07	0.33	0.32	$y=1.096x^{0.386}$	0.83	1.9e-06	0.33	0.23
D_{95}	$y=24.781x^{0.398}$	0.84	8.0e-08	0.29	0.26	$y=1.35x^{0.338}$	0.76	8.9e-06	0.36	0.28

Table 4: Statistical relationships between the percentiles of the distributions of the Rh metric and the standard deviation of the intensity values and the GSD of the field pebble counts. The RMSE and MAE metrics are in psi. NE corresponds to no estimation.

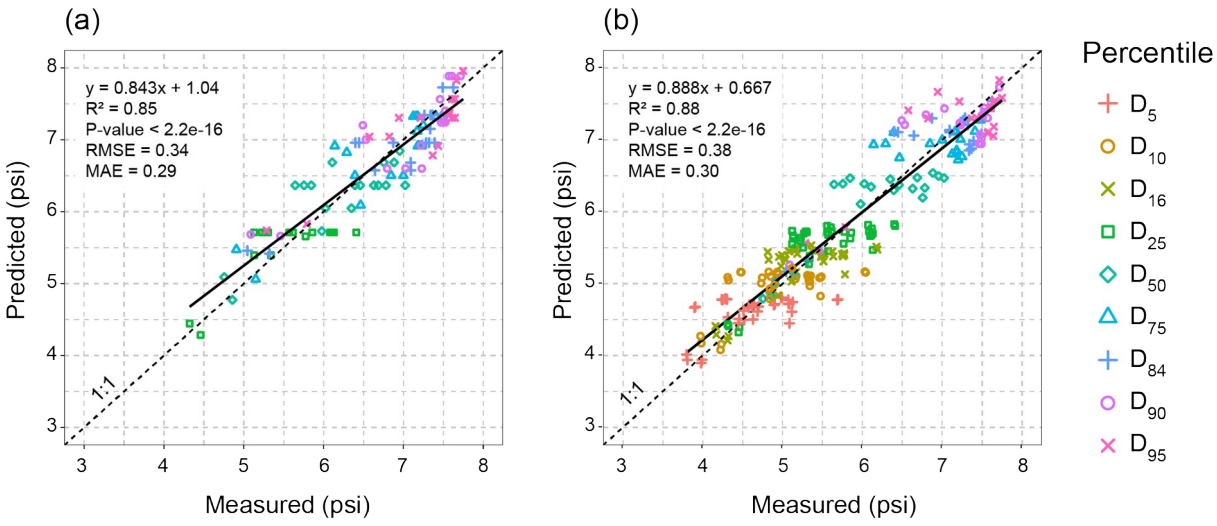
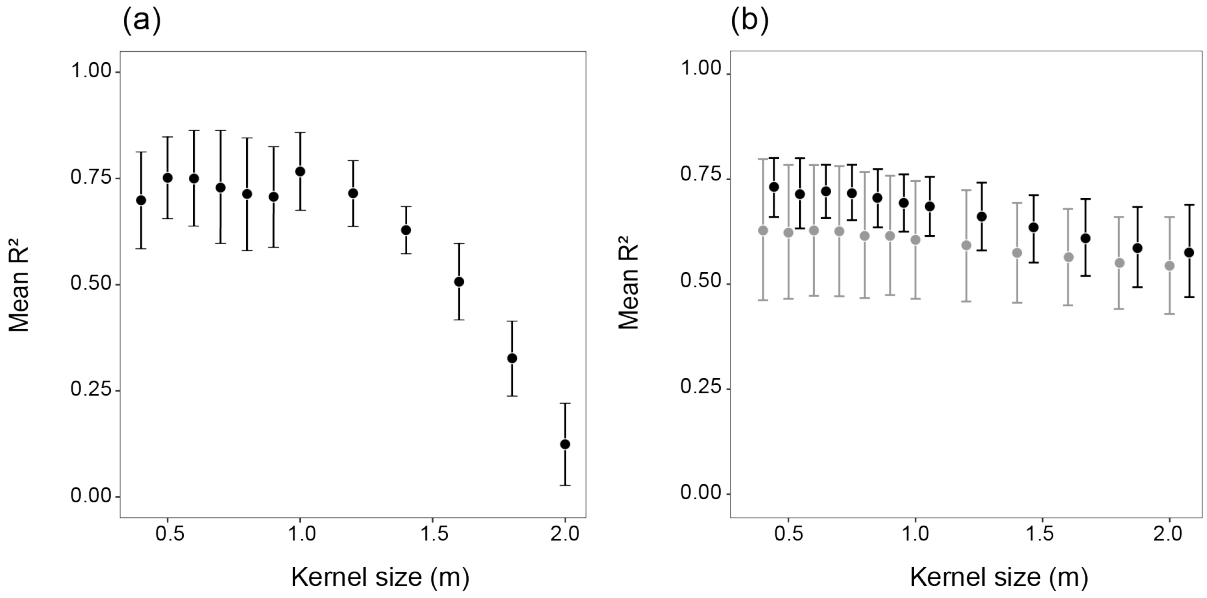


Figure 10: Predicted percentiles by (a) the Rh metric and (b) the standard deviation of the intensity values for different percentiles.

3.2.2 Effects of the kernel size computation

Figure 11.a shows the evolution of the R^2 coefficient of the relation between the percentiles of the distribution of the Rh metric and the GSD of the field pebble counts as a function of the kernel size computation of the metric. The relations were strong with a mean R^2 coefficient ranging from 0.64 to 0.77 in a range of kernel sizes from 0.4 m to 1.2 m and decreased for a kernel size equal to 1.4 m (Figure 11.a). The best correlation was found for a kernel size equal to 1.0 m, which corresponds to three to four times the B-axis of the largest particle. Figure 11.b shows the evolution of the R^2 coefficient of the relation between the percentiles of the distribution of the standard deviation of the intensity values and the GSD of the field pebble counts as a function of the kernel size computation of the metric. A small decrease in the mean R^2 coefficient from 0.72 to 0.62 was observed for a kernel size increasing from 0.1 to 2.0 m. The highest R^2 was found for a kernel size equal to 0.4 m (grain size ranging between the 25th and 95th percentiles). For the percentiles ranging between the 5th and 95th percentiles, R^2 decreases from 0.62 to 0.58 when the kernel size increases

460 from 0.1 to 2.0 m. No clear threshold of kernel size appears for the standard
461 deviation of the intensity, contrary to the Rh metric.



462

463 Figure 11: Impact of the kernel size used for the computation of the two proxies for
464 (a) the Rh metric and (b) the standard deviation of the intensity values on the
465 statistical relationships between the distribution of the metrics and the GSD of the
466 field pebble count. Black points correspond to the mean values of R^2 from the 25th to
467 the 95th percentiles; the gray points correspond to the mean values of R^2 for the 5th to
468 the 95th percentiles. Error bars correspond to +/- one standard deviation.

469 3.2.3 Effect of sediment characteristics

470 Figure 12 compares the relation between the 84th percentile of the GSD of the field
471 pebble counts and the 84th percentile of the Rh metric distribution found in this study
472 with that found in the literature. The equation slopes show a large variability,
473 indicating that multiple values of the Rh metric can be found in the same grain size
474 range. Vázquez-Tarrío et al., (2017) found a relation close to the 1:1 line with a slope
475 value equal to 0.79, while Woodget et al., (2017) found a very high slope equal to

12.35. Our empirical relation is enclosed between these two relations with a slope value equal to 6.46.

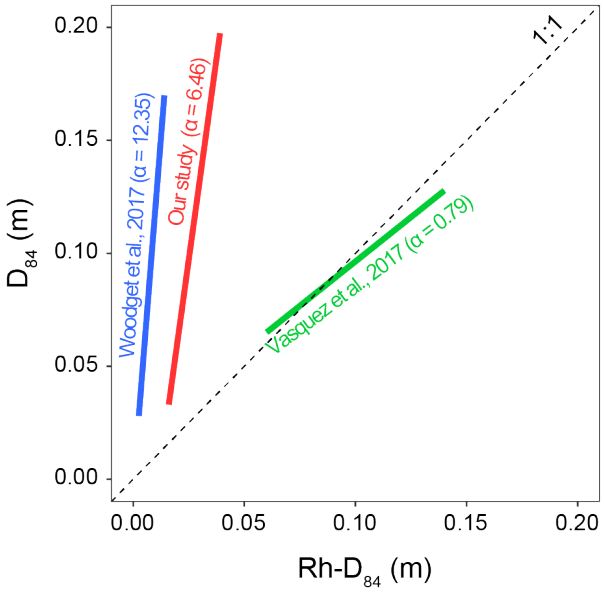


Figure 12: Relation between the 84th percentile of the field pebble-count distribution according to the 84th percentile of the distribution of the Rh metric compared with the literature results. The calibration of Woodget et al., (2017) was based on a grid count on ground digital images (0.4 m x 0.4 m), whereas Vázquez-Tarrío et al., (2017) used field pebble counts. Values of α correspond to the slope of the linear relations found between the two variables.

3.2.4 Computation of the predicted grain size maps

Figure 13 shows the predicted maps of the median grain size at the cell scale (1 m x 1 m) from the standard deviation of the intensity values (Figure 14.a) and Rh metric (Figure 14.b). The maps show similar spatial predictions of the grain size patterns with bed refinement in the downstream direction and from the thalweg to the bank direction, which are generally observed on above-water bars and in accordance with our qualitative field observations. However, the relationship obtained by the standard deviation of the intensity values shows a lower spatial variability than that obtained

with the Rh metric. Significant differences exist in the predicted 84th percentile between the two proxies with a standard deviation of the difference equal to 0.78 psi (Figure 13.c).

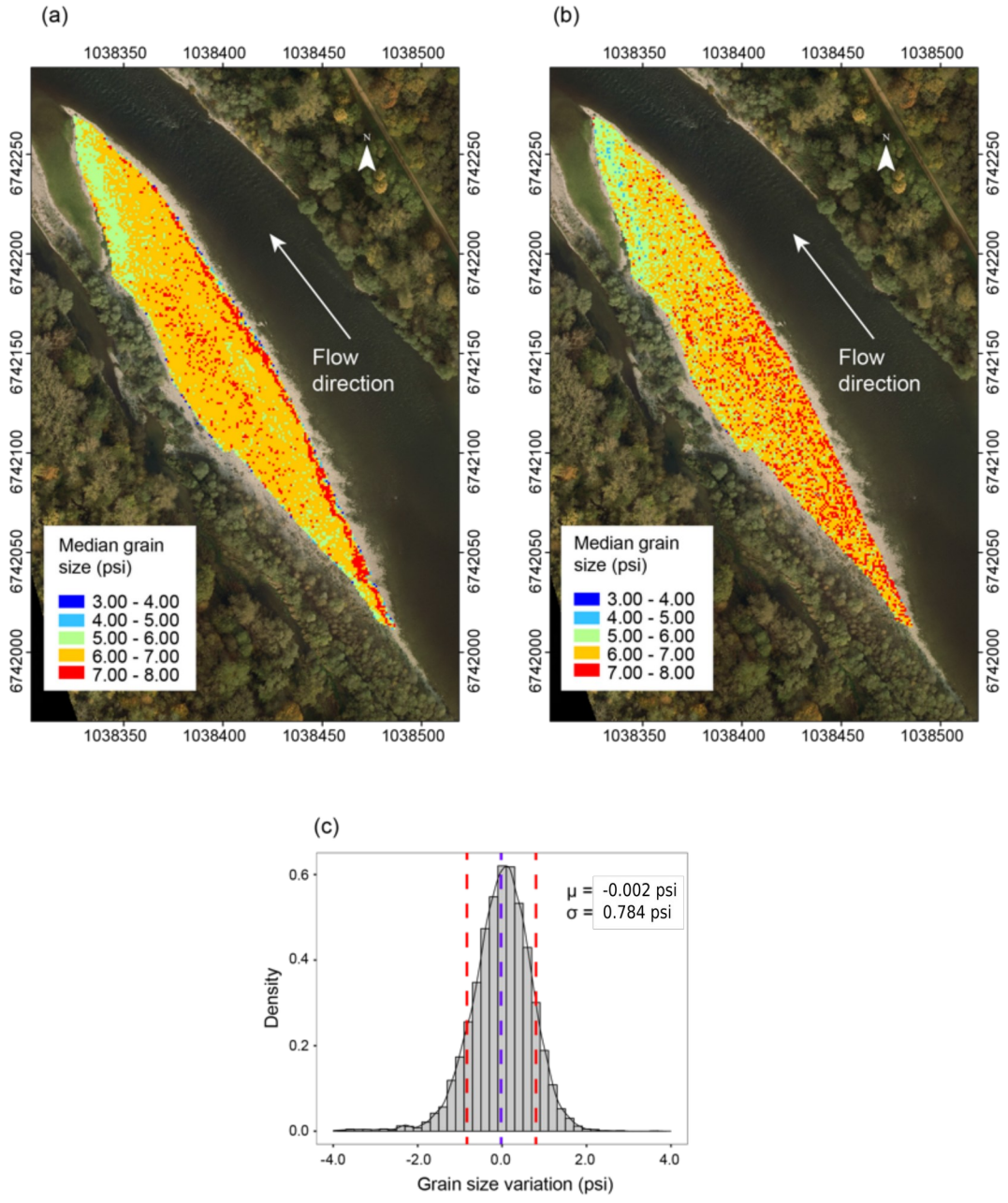
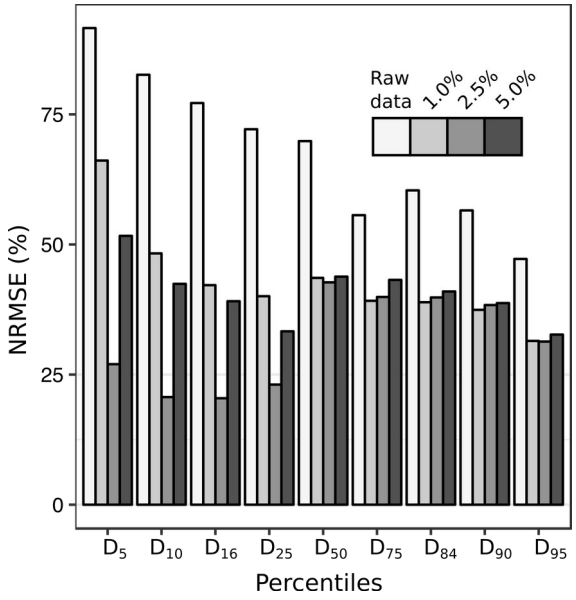


Figure 13: Predicted maps of the median grain size on an above-water bar by using (a) the standard deviation of the intensity values and (b) the Rh metric as a proxy. The differences in the predictions between the two proxies are given in (c). The blue and red dashed lines correspond to the mean and +/- 1 standard deviation of the differences between the two metrics, respectively.

3.3 Accuracy of the GSD estimation in underwater conditions by terrestrial photosieving

3.3.1 The automatic procedure

The results showed that the accuracy of the GSD estimated by DGS software was dependent on the type of substrate. Low values of the NRMSE were obtained for clean substrate, while the NRMSE values exceeded 40% for all percentiles for substrate with the presence of biofilm (Table 2). For both types of substrate, the NRMSE decreased when the percentiles increased. Low values of the NRMSE for clean substrate are explained by low particle intravariability and high particle intervariability, whereas high NRMSE values for substrate with the presence of biofilm and/or presence of deposition are due to both low particle intravariability and intervariability of gray values (Figure 5). Considering sensitivity analyses, the best kernel size for digital image computation with the presence of biofilm to significantly reduce error estimations by the DGS software is equal to 2.5% of D_{max} (Figure 14, Table 2). In this case, the median filter increases the intervariability between the particles (Figure 5). However, the NRMSE values are still too high to use DGS software to estimate the GSD for substrate with biofilms (Table 2).

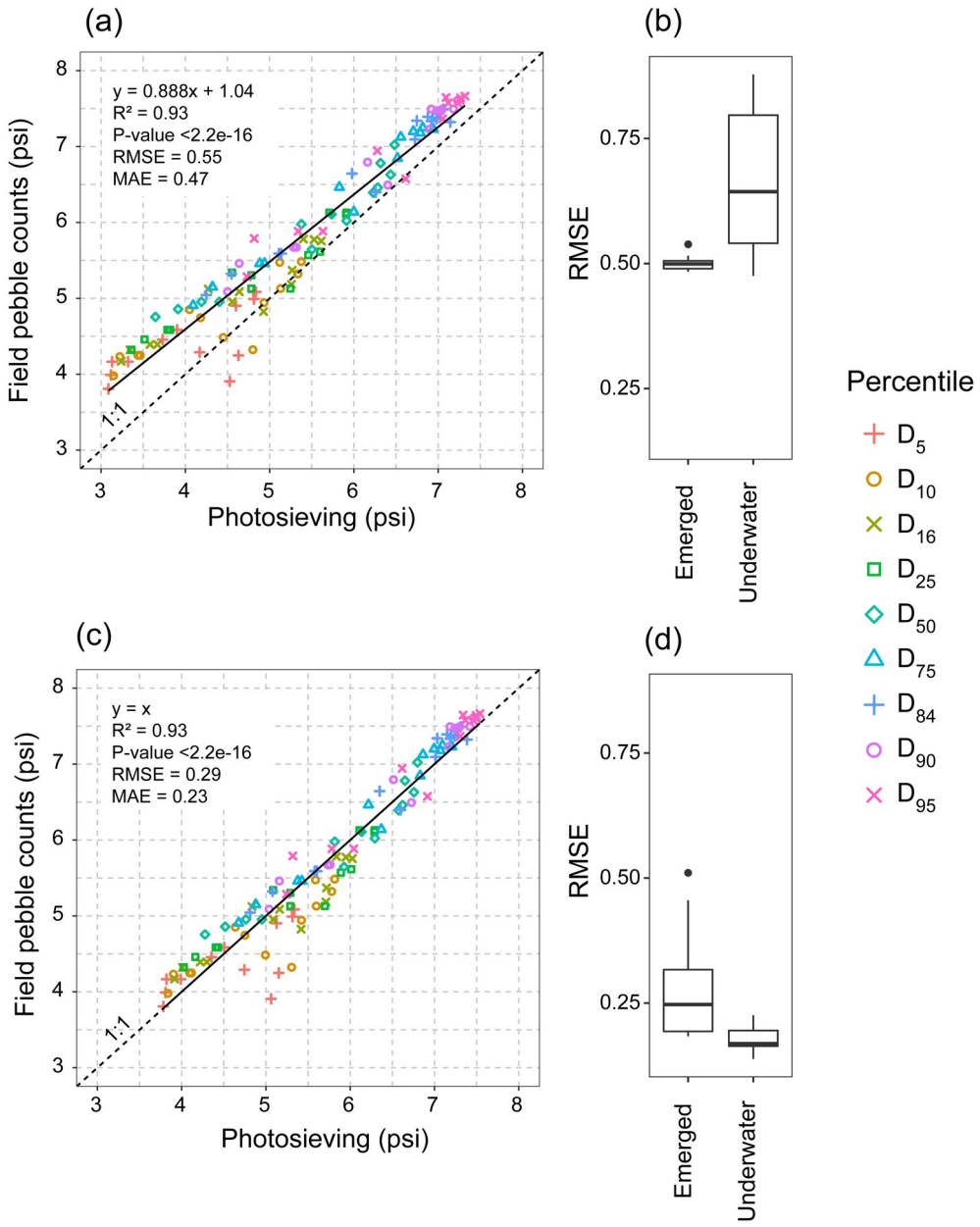


526

527 Figure 14: Effect of the application of the median filter on the NRMSE values for each
528 percentile according to the kernel size computation. Percentages correspond to the
529 kernel size of the median filter divided by the B-axis of the largest particle multiplied
530 by 100.

531 3.3.2 Exploring manual processing of ground digital images to process all contexts

532 Manual processing was tested because the majority of the digital images collected in
533 underwater conditions were impacted by the presence of biofilm, notably due to
534 relatively low bedload mobility along the study reach. The manual method offers the
535 advantage of being less influenced by environmental conditions than the automatic
536 procedure (see section 3.1.2). Similar to the automatic procedure, an
537 underestimation of the field pebble count was observed with the manual procedure in
538 both above-water and underwater conditions (Figure 15.a). The bias was corrected
539 by a linear regression (Figure 15.c), inducing a significant reduction in the RMSE in
540 both conditions that was equivalent for both environmental recording conditions
541 (Figure 15.b-d).



542

543 Figure 15: (a) Manual procedure before the bias correction, (b) boxplots of the RMSE
544 values before the bias correction for each environmental recording condition, (c)
545 manual procedure after the bias correction and (d) boxplots of the RMSE values after
546 bias correction for each environmental recording condition. Black lines correspond to
547 the linear regression, and dashed lines correspond to the 1:1 relation. The RMSE
548 and MAE values are in psi, and n corresponds to the number of field pebble counts.

4. Discussion

4.1 Above-water conditions

4.1.1 Accuracy of terrestrial photosieving and airborne topographic LiDAR to estimate the GSD in above-water conditions

Our results demonstrate that both terrestrial photosieving and proxies extracted from the airborne topographic LiDAR are reliable for estimating the GSD in above-water conditions once calibrated. Differences between the results of the two procedures suggest that terrestrial photosieving is more accurate than the Rh metric and standard deviation of intensity values extracted from the airborne topographic LiDAR data (Table 3, Table 4). This can be explained by the fact that photosieving estimates grain size in the plan view, which is less affected by sediment patch imbrication than three-dimensional views (Carbonneau et al., 2005; Woodget et al., 2018).

The automatic procedure of the digital images systematically underestimated the GSD of the field pebble counts, as also reported by Sime & Ferguson, (2003), Strom et al., (2010) and Warrick et al., (2009), but it can be corrected by simple linear regressions (Figure 8). This underestimation by photosieving is explained by burial, overlapping, foreshortening and the C-axis not being oriented perpendicularly to the plane of some particles (Graham et al., 2010). The irreducible errors found in this study are in the same range as those in other studies (Table 3).

Comparison between the two proxies extracted from the airborne topographic LiDAR survey shows that the standard deviation of intensity seems to predict the GSD with higher accuracy than does the Rh metric and allows an estimation of the low percentiles of the distribution, contrary to the Rh metric. We explain this by the fact that the intensity values are less affected by recording uncertainties (Table 1). The comparison of our results with previous studies shows a large variability in the

empirical relationships between the Rh metric (D_{84}) and GSD (D_{84}) for the same range of grain sizes (Figure 12). Our empirical relation is located between the relations of Woodget & Austrums, (2017) and Vázquez-Tarrío et al., (2017). Pearson et al., (2017) showed that bed roughness is influenced by several parameters, including the shape of particles, packing and bed imbrication of particles, and distribution shape and survey errors, and can explain differences in roughness values for the same range of grain sizes. Vázquez-Tarrío et al., (2017) reported that their sediment patches were composed of well-rounded and subspherical granitic and metamorphic gravels and cobbles. In our case, particles were mostly flat and imbricated, generating lower roughness values for a given GSD. Woodget & Austrums, (2017) also reported that their sediment patches were mostly composed of packed and imbricated particles. As intensity values are dependent on the bed surface roughness, it is very likely that various relationships could also be found between the standard deviation of the intensity values and the bed grain size for the same range of GSD. The approach of Pearson et al., (2017) in laboratory conditions with the objective of assessing the influence of the sedimentary characteristics on the roughness - grain size relationship could also be performed in the field to try to build an abacus and derive from it several universal calibration laws usable for the two methods based on LiDAR data. It should be noted that this technique is limited only to sections of rivers where the roughness is relatively high and higher than the georeferenced error of the survey along the z-dimension.

Both methods have their own advantages: terrestrial photosieving allows the GSD to be followed at a high temporal frequency with rapid grain size information and is cheaper, whereas airborne topographic LiDAR can predict the GSD in large above-

598 water areas and produce grain size maps, which is crucial to surveying the grain size
599 evolution, notably for restorations along large rivers (Figure 13).

600 4.1.2 Toward an optimization of the two methods

601 Our study reveals that the accuracy of the automatic procedure of digital images to
602 estimate the GSD is dependent on both the environmental conditions and the
603 sampling area. The higher NRMSE values in our study compared to those published
604 by Buscombe (2013) may be explained by the petrographic variability of the particles,
605 which induces oversegmentation due to high intravariability of the gray values of
606 pixels (Figure 5). However, the use of a median filter can significantly reduce the
607 oversegmentation with a decrease in the NRMSE value, close to the results of
608 Buscombe (2013). Moreover, our study shows that DGS estimations were influenced
609 by solar lighting in the majority of the cases with an underestimation using sunny
610 photographs by comparison with photographs with shadow conditions. Changes in
611 underestimation values are explained by the changes in the solar angle during a day.
612 These observations are in accordance with Warrick et al., (2009) and may be
613 explained by the fact that bed roughness generated by the coarser particles induced
614 large shadow areas in low sun angles Warrick et al., (2009) and explain why low
615 percentiles were more impacted by solar conditions than were coarse percentiles.
616 Thus, the variation in solar lighting conditions can alter the calibration step between
617 the GSD estimated by digital images and the field pebble counts. In addition, our
618 study reveals that sensitivity analyses must be conducted to define the minimal
619 sampling area from which the fluctuation of the DGS software becomes low to
620 minimize variability during the calibration step with the field pebble counts. For our
621 sediment patches, our study reveals that fluctuations were significantly reduced for a
622 sampling area 80 times larger than the largest particle area. This sampling area is

623 dependent on the sorting index of the sampling sediment patches (Figure 7), but
624 other parameters of the distribution shape (e.g., skewness, bimodality) can also
625 influence the accuracy for a given surface sampling (Rice & Church, 1996).
626 For the airborne topographic LiDAR, our study highlights that the accuracy of the Rh
627 metric to predict the GSD can be dependent on the kernel size computation, contrary
628 to the standard deviation of the intensity values, which requires no presensitivity
629 analysis and significantly reduces the processing time (Figure 11).
630 The best kernel size to compute the Rh metric is four times larger than Dmax, which
631 is twice the values found by Vázquez-Tarrío et al., (2017). We hypothesize that this
632 difference is the consequence of a lower point density in our study (38 to 49/m^2)
633 compared to that of Vázquez-Tarrío et al., (2017; 36 to 1052/m^2).
634 Supplementary research is needed to evaluate the impact of the density of the point
635 cloud on the reliability of the bed GSD estimation by the intensity metric. Vázquez-
636 Tarrío et al., (2017) showed that 10 pts/m^2 is the minimal threshold to estimate the
637 bed GSD by the Rh metric with accuracy for their range of sediment sizes. Research
638 must also be conducted to evaluate the influence of the spot size of the beam, which
639 depends both on the flight elevation and on the open angle of the captor.

640 **4.2 Underwater conditions: accuracy of digital images**

641 Our results show that the automatic procedure is a reliable method to estimate the
642 GSD for clean substrate. Contrary to above-water conditions, there is no need to
643 apply a median filter to reduce estimation errors by the DGS software. This is
644 explained by the absorption of solar light by the water column, which significantly
645 reduces the variability of the gray values on the digital images, thus minimizing the
646 oversegmentation by the DGS software. However, this method does not allow
647 substrate with biofilms to be processed even with the application of a median filter for

percentiles equal to and greater than the 50th percentile. An alternative approach must be conducted to process this kind of data, as this situation is very frequent for rivers with weak bedload dynamics and/or with high wash loads. The manual approach proposed in this paper is a reliable method to estimate the GSD of substrate with biofilms and has the advantages of requiring no preprocessing step and is independent of environmental conditions (Figure 15). This approach can also be applied in above-water conditions if photosieving was conducted in limiting environmental conditions (e.g., solar light for calibration purposes with field pebble counts, local growth of small pioneer vegetation). Unfortunately, it presents a nonnegligible operator-introduced bias during the manual B-axis determination.

4.3 Methodological recommendations

To perform data calibration from terrestrial photosieving with field pebble counts in above-water conditions, we recommend the following:

(i) Collect the dataset during cloudy days as proposed by (Warrick et al., 2009; Buscombe et al., 2010) and when the vegetation is not yet developed (Graham et al., 2005b).

(ii) Use a median filter in case of large variability in particle petrography to reduce the oversegmentation by the DGS software. The best kernel size for the median filter computation found in this study can vary as a function of the petrographic characteristics of the sediment patches studied; thus, new sensitivity analyses must be conducted for studies performed on other rivers.

(iii) Perform sensitivity analyses to evaluate the minimal sampling area from which the estimation fluctuations of the DGS software are judged to be low in relation to the characteristics of sediment patches studied.

To perform data calibration from the two metrics extracted from the airborne topographic LiDAR survey with the field pebble counts in above-water areas, we recommend the following:

(i) Prioritize the dataset collection in winter due to the absence of vegetation to limit estimation errors during the computation of the two metrics and evaluate the GSD on the largest possible area. Preferentially use the standard deviation of the intensity values rather than the Rh metric because the accuracy prediction of the metric is weakly dependent on the kernel size computation of the metric and reduces processing time.

(ii) In the case when intensity values are not available, the Rh metric can be a useful proxy, but sensitivity analyses must be performed to find the best size of the kernel computation of the metric.

The relationships found in this study have been performed for a maximum beam size equal to 12 cm and a minimal density of points greater than 30 pts/m^2. Supplementary research should be conducted to evaluate the influence of these parameters on the relation between the two proxies tested in this study and the bed GSD.

For digital image collection in underwater conditions, we recommend the following:

(i) Perform a survey once the water turbidity is low and biofilm is not yet developed as during low water temperature or just after critical flood events.

(ii) Collect the data by using the video option of the camera rather than the photographs option to limit blurred images due to the movement of the boat, which does not allow the captor to make the adjustment and requires less time in the field.

698 We used between ten and twenty field data calibrations for the two methods used in
699 this study deployed along several kilometers of river reach. However, the number of
700 these survey calibrations may be higher for studies covering several tens of
701 kilometers because the heterogeneity of the GSD may be relatively important due to
702 various sedimentary contexts (e.g., influence of tributaries, bedload inputs, contacts
703 with lateral hillslope), which can generate various sediment patch characteristics
704 (Vázquez-Tarrío et al., 2017).

705 5. Conclusion

706 This study highlights the ability of terrestrial photosieving and, for the first time, the
707 capacity of airborne topographic LiDAR surveys based on the computation of two
708 metrics, the Rh metric and the standard deviation of the intensity values, to estimate
709 the GSD of above-water deposits. The errors of both methods are similar with a
710 range of MAE values from 0.23 to 0.31 psi. Airborne topographic LiDAR allows the
711 production of maps of the GSD, while rapid GSD estimations can be produced only
712 by terrestrial photosieving. The results also show that the accuracy of automatic
713 processing of terrestrial photosieving depends on the environmental conditions and
714 areal sampling. For both proxies derived from airborne topographic LiDAR, the
715 accuracy of the predicted GSD for the Rh metric is dependent on the size of the
716 kernel computation, contrary to the standard deviation of the intensity values. The
717 latter allows the estimation of all grain size percentiles, whereas the Rh metric allows
718 the estimation of only the grain size percentiles coarser than the 25th due to the
719 larger uncertainties of recording. The automatic procedure of terrestrial photosieving
720 is also a reliable method to estimate the GSD in underwater conditions for clean
721 substrates, but it cannot be adapted in the presence of biofilm. The manual
722 procedure can be a relevant alternative to overcome these constraints. Thus,

combining terrestrial photosieving with airborne topographic LiDAR appears a relevant compromise for surveying the GSD in large rivers, along reaches of several kilometers and over the whole channel cross section with rapid GSD data in underwater conditions and continuous GSD data in above-water conditions. In the future, one important challenge is to develop universal laws according to sediment patch characteristics for both terrestrial photosieving and airborne topographic LiDAR surveys.

References

Fanny A. 2012. “Approches Géomorphologiques Historique et Expérimentale Pour La Restauration de La Dynamique Sédimentaire d’ Un Tronçon Fluvial Aménagé : Le Cas Du Vieux Rhin Entre Kembs et Breisach (France, Allemagne),” 1–280.

Barnard PL, Rubin DM, Harney J, and Mustain N. **2007. “Field Test Comparison of an Autocorrelation Technique for Determining Grain Size Using a Digital ‘beachball’ Camera versus Traditional Methods.” *Sedimentary Geology* 201 (1–2): 180–95. https://doi.org/10.1016/j.sedgeo.2007.05.016.**

Bizzi S, Piégay H, Demarchi L, Van de Bund W, Weissteiner CJ, and F. Gob F. 2019. “LiDAR-Based Fluvial Remote Sensing to Assess 50–100-Year Human-Driven Channel Changes at a Regional Level: The Case of the Piedmont Region, Italy.” *Earth Surface Processes and Landforms* 44 (2): 471–89. https://doi.org/10.1002/esp.4509.

Black M, Carbonneau P, Church M, and Warburton J. **2014. “Mapping Sub-Pixel Fluvial Grain Sizes with Hyperspatial Imagery.” *Sedimentology* 61 (3): 691–711. https://doi.org/10.1111/sed.12072.**

Brasington J, Vericat D, and Rychkov I. 2012. “Modeling River Bed Morphology, Roughness, and Surface Sedimentology Using High Resolution Terrestrial Laser Scanning.” *Water Resources Research* 48 (11): 1–18. https://doi.org/10.1029/2012WR012223.

Bunte K, and Abt SR 2001. “Sampling Surface and Subsurface Particle-Size Distributions in Wadable Gravel- and Cobble-Bed Streams for Analyses in Sediment Transport , Hydraulics , and Streambed Monitoring.” *0*, no. August: 450. https://doi.org/10.1017/CBO9781107415324.004.

Buscombe D, Grams PE, and Kaplinski MA. 2017. “Compositional Signatures in Acoustic Backscatter Over Vegetated and Unvegetated Mixed Sand-Gravel Riverbeds.” *Journal of Geophysical Research: Earth Surface* 122 (10): 1771–93. https://doi.org/10.1002/2017JF004302.

Buscombe D. 2010. “An Automated and Universal Method for Measuring Mean Grain Size.” *Sedimentary Geology* 210 (1–2): 1–10. https://doi.org/10.1016/j.sedgeo.2008.06.007.

Buscombe D. 2013. “Transferable Wavelet Method for Grain-Size Distribution from Images of Sediment Surfaces and Thin Sections, and Other Natural Granular Patterns.” *Sedimentology* 60 (7): 1709–32. https://doi.org/10.1111/sed.12049.

Buscombe D, Grams PE and Smith MC. 2015. “Automated Riverbed Sediment Classification Using Low-Cost Sidescan Sonar.” *ASCE Journal of Hydraulic Engineering* 138 (July): 642–52. https://doi.org/10.1061/(ASCE)HY.1943-7900.

Butler JB, Lane SN, and Chandler JH. 2001. “Automated Extraction of Grain-Size Data from Gravel Surfaces Using Digital Image Processing.” *Journal of*

Hydraulic Research 39 (5): 519–29. https://doi.org/10.1080/00221686.2001.9628276.

Carbonneau PE, Bergeron N, and Lane SN. 2005. "Automated Grain Size Measurements from Airborne Remote Sensing for Long Profile Measurements of Fluvial Grain Sizes." *Water Resources Research* 41 (11): 1–9. https://doi.org/10.1029/2005WR003994.

Carbonneau PE, Lane SN, and Bergeron NE. 2004. "Catchment-Scale Mapping of Surface Grain Size in Gravel Bed Rivers Using Airborne Digital Imagery." *Water Resources Research* 40 (7). https://doi.org/10.1029/2003WR002759.

Carbonnneau PE, Bizzi S, and Marchetti G. 2018. "Robotic Photosieving from Low-Cost Multirotor SUAS: A Proof-of-Concept." https://doi.org/10.1002/esp.4298.

Charlton ME, Large RG, and Fuller IC. 2003. "Application of Airborne Lidar in River Environments: The River Coquet, Northumberland, UK." *Earth Surface Processes and Landforms* 28 (3): 299–306. https://doi.org/10.1002/esp.482.

Church MA, Mclean DG, and Wolcott JF. 1987. "River Bed Gravels: Sampling and Analysis."

Demarchi L, Bizzi S, and Piégay H. 2016. "Hierarchical Object-Based Mapping of Riverscape Units and in-Stream Mesohabitats Using Lidar and VHR Imagery." *Remote Sensing* 8 (2). https://doi.org/10.3390/rs8020097.

Detert M, and Weitbrecht V. 2012. "Automatic Object Detection to Analyze the Geometry of Gravel Grains–a Free Stand-Alone Tool." *River Flow 2012*, no. August 2016: 595–600.

http://people.ee.ethz.ch/~vawweb/publications/river_engineering_division_vaw/2012_3125.pdf.

Dugdale SJ, Carbonneau P, and Campbell D. 2010. “Aerial Photosieving of Exposed Gravel Bars for the Rapid Calibration of Airborne Grain Size Maps.” *Earth Surface Processes and Landforms* 35 (6): 627–39. https://doi.org/10.1002/esp.1936.

Fernandez-Diaz JC, William E. Carter WE, Craig Glennie C, Shrestha RL, Zhigang P, Ekhtari N, Singhania A, Hauser D, and Sartori M. 2016. “Capability Assessment and Performance Metrics for the Titan Multispectral Mapping Lidar.” *Remote Sensing* 8 (11): 1–33. https://doi.org/10.3390/rs8110936.

Graham DJ, Reid I, and Rice SP. 2005. “Automated Sizing of Coarse-Grained Sediments : Image-Processing Procedures.” Loughborough University Institutional Repository, vol.37, 28p.

Graham DJ, Rice SP, and Reid I. 2005. “A Transferable Method for the Automated Grain Sizing of River Gravels.” *Water Resources Research* 41 (7): 1–12. https://doi.org/10.1029/2004WR003868.

Graham, DJ, Rollet AJ, Piégay H, and Rice SP. 2010. “Maximizing the Accuracy of Image-Based Surface Sediment Sampling Techniques.” *Water Resources Research* 46 (2): 1–15. https://doi.org/10.1029/2008WR006940.

Hamill D, Buscombe D, and Wheaton JM. 2018. “Alluvial Substrate Mapping by Automated Texture Segmentation of Recreational-Grade Side Scan Sonar Imagery.” *PLoS ONE* 13 (3). https://doi.org/10.1371/journal.pone.0194373.

Heritage GL, and Milan DJ. 2009. “Terrestrial Laser Scanning of Grain Roughness in a Gravel-Bed River.” *Geomorphology* 113 (1–2): 4–11.

https://doi.org/10.1016/j.geomorph.2009.03.021.

Ibbeken H, and Schleyer R. 1986. “Photo-sieving: A Method for Grain-size Analysis of Coarse-grained, Unconsolidated Bedding Surfaces.” *Earth Surface Processes and Landforms*. https://doi.org/10.1002/esp.3290110108.

Kaasalainen S, Jaakkola A, Kaasalainen M, Krooks A, and Kukko A. 2011. “Analysis of Incidence Angle and Distance Effects on Terrestrial Laser Scanner Intensity: Search for Correction Methods.” *Remote Sensing* 3 (10): 2207–21. https://doi.org/10.3390/rs3102207.

Kadi Abderrezzak Kamal El. 2009. “Report H-P73-2009-00402-FR,” 1–26.

Kashani AG, Olsen MJ, Parrish CE, and Wilson N. 2015. “A Review of LIDAR Radiometric Processing: From Ad Hoc Intensity Correction to Rigorous Radiometric Calibration,” 28099–128. https://doi.org/10.3390/s151128099.

Kellerhals R, and Bray DI. 1971. “Sampling Procedures for Coarse Fluvial Sediments.” *Journal of the Hydraulics Division, ASCE*.

Kukko A, Kaasalainen S, and Litkey P. 2008. “Effect of Incidence Angle on Laser Scanner Intensity and Surface Data.” *Applied Optics* 47 (7): 986. https://doi.org/10.1364/AO.47.000986.

Lague D , Brodu N, and Leroux J. 2013. “Accurate 3D Comparison of Complex Topography with Terrestrial Laser Scanner: Application to the Rangitikei Canyon (N-Z).” *ISPRS Journal of Photogrammetry and Remote Sensing* 82 (February 2013): 10–26. https://doi.org/10.1016/j.isprsjprs.2013.04.009.

Lejot J, Piégay H, Hunter PD, Moulin B, and Gagnage M. 2011. “Utilisation de La Télédétection Pour La Caractérisation Des Corridors Fluviaux : Exemples d ’ Applications et Enjeux Actuels Characterisation of Alluvial Plains by Remote Sensing : Cases Studies and Current Stakes” 09.

Li D, Wang C, Luo SZ, and Zuo ZL. 2015. “Airborne Lidar Intensity Calibration and Application for Land Use Classification” 9262 (9): 926212–19. https://doi.org/10.1117/12.2069014.

Lucas HJ, and Strom KB. 1987. “Comparison of Automated Grain Sizing of Gravel Beds Using Digital Images to Standard Grid and Random-Walk Pebble Counts.” *Rsmsl-1.Me.Uh.Edu*, 1–14. http://rsmsl-1.me.uh.edu/reu_civil/REU08/Heather Lucas/REU Report - Comparison of Automated Grain Sizing of Gravel Beds Using Digital Images to Standard Grid and Random-walk Pebble Counts.pdf.

MacKenzie LG, Eaton BC, and Church M. 2018. “Breaking from the Average: Why Large Grains Matter in Gravel Bed Streams.” *Earth Surface Processes and Landforms*. https://doi.org/10.1002/esp.4465.

Mandlburger G, Hauer C, Wieser M, and Pfeifer N. 2015. “Topo-Bathymetric LiDAR for Monitoring River Morphodynamics and Instream Habitats-A Case Study at the Pielach River.” *Remote Sensing* 7 (5): 6160–95. https://doi.org/10.3390/rs70506160.

Marteau B, Vericat D, Gibbins C, Batalla RJ, and Green DR. 2017. “Application of Structure-from-Motion Photogrammetry to River Restoration.” In *Earth Surface Processes and Landforms*, 42:503–15. https://doi.org/10.1002/esp.4086.

McEwan IK, Sheen TM, Cunningham GJ, and Allen AR. 2000. “Estimating the Size Composition of Sediment Surfaces through Image Analysis.” *Proceedings of the Institution of Civil Engineers - Water and Maritime Engineering* 142 (4): 189–95. https://doi.org/10.1680/wame.2000.142.4.189.

Pearson E, Smith MW, Klaar MJ, and Brown LE. 2017. “Can High Resolution 3D

Topographic Surveys Provide Reliable Grain Size Estimates in Gravel Bed Rivers?" *Geomorphology* 293 (March): 143–55. https://doi.org/10.1016/j.geomorph.2017.05.015.

Petrie J, and Diplas P. 2000. "Statistical Approach to Sediment Sampling Accuracy." *Water Resources Research* 36 (2): 597–605. https://doi.org/10.1029/1999WR900321.

Rainey MP, Tyler AN, Gilvear DJ, Bryant RG, and McDonald P. 2003. "Mapping Intertidal Estuarine Sediment Grain Size Distributions through Airborne Remote Sensing." *Remote Sensing of Environment* 86 (4): 480–90. https://doi.org/10.1016/S0034-4257(03)00126-3.

Reymann C, and Lacroix S. 2015. "Improving LiDAR Point Cloud Classification Using Intensities and Multiple Echoes To Cite This Version : HAL Id : Hal-01182604 Improving LiDAR Point Cloud Classification Using Intensities and Multiple Echoes."

Rice SP, and Church M. 1996. "Sampling surficial fluvial gravels: the precision of size distribution percentile estimates."Journal of Sedimentary Research 66(3):654-665

Rüther N. 2013. "Verifying a Photogrammetric Method to Quantify Grain Size Distribution of Developed Armor Layers," no. September 2014.

Schmitt L, Morris D, and Kondolf GM. 2018. "Managing Flood Risk: Innovative Approaches from Big Floodplain Rivers and Urban Streams." *Managing Flood Risk: Innovative Approaches from Big Floodplain Rivers and Urban Streams*, 1–164. https://doi.org/10.1007/978-3-319-71673-2.

Shaker A, Yeung Yan W, and LaRocque PE. 2019. "Automatic Land-Water Classification Using Multispectral Airborne LiDAR Data for near-Shore and

River Environments.” *ISPRS Journal of Photogrammetry and Remote Sensing* 152 (July 2018): 94–108. https://doi.org/10.1016/j.isprsjprs.2019.04.005.

Sime LC, and Ferguson RI. 2003. “Information on Grain Sizes in Gravel-Bed Rivers by Automated Image Analysis.” *Research Methods Papers* 73 (4): 630–36. https://doi.org/10.1306/112102730630.

Storz-Peretz Y, and Laronne JB. 2013. “Morphotextural Characterization of Dryland Braided Channels.” *Bulletin of the Geological Society of America* 125 (9–10): 1599–1617. https://doi.org/10.1130/B30773.1.

Strom KB, Kuhns RD, and Lucas HJ. 2010. “Comparison of Automated Image-Based Grain Sizing to Standard Pebble-Count Methods.” *Journal of Hydraulic Engineering* 136 (8): 461–73. https://doi.org/10.1061/(ASCE)HY.1943-7900.0000198.

Sulaiman MS, Sinnakaudan SK, Ng SF, and Strom K. 2014. “Catena Application of Automated Grain Sizing Technique (AGS) for Bed Load Samples at Rasil River : A Case Study for Supply Limited Channel” 121: 330–43. https://doi.org/10.1016/j.catena.2014.05.013.

Uehlinger U, and Wantzen KM. 2009. "*The Rhine River Basin*". River of Europe, pp 199-245.

Vázquez-Tarrío D, Borgniet L, Liébault F, and Recking A. 2017. “Using UAS Optical Imagery and SfM Photogrammetry to Characterize the Surface Grain Size of Gravel Bars in a Braided River (Vénéon River, French Alps).” *Geomorphology* 285: 94–105. https://doi.org/10.1016/j.geomorph.2017.01.039.

Verdú JM, Batalla RJ, and Martínez-Casasnovas JA. 2005. “High-Resolution

Grain-Size Characterisation of Gravel Bars Using Imagery Analysis and Geo-Statistics." *Geomorphology* 72 (1–4): 73–93. https://doi.org/10.1016/j.geomorph.2005.04.015.

Warrick JA, Rubin DM, Ruggiero P, Harney JN, Draut AE, and Buscombe D. 2009. "Cobble Cam: Grain-Size Measurements of Sand to Boulder from Digital Photographs and Autocorrelation Analyses." *Earth Surface Processes and Landforms* 34 (13): 1811–21. https://doi.org/10.1002/esp.1877.

Wolman MG. 1954. "A Method of Sampling Coarse River-Bed Material."

Woodget AS, Fyffe C, and Carbonneau PE. 2018. "From Manned to Unmanned Aircraft: Adapting Airborne Particle Size Mapping Methodologies to the Characteristics of SUAS and SfM." *Earth Surface Processes and Landforms*, 2018. https://doi.org/10.1002/esp.4285.

Woodget AS, and Austrums R. 2017. "Subaerial Gravel Size Measurement Using Topographic Data Derived from a UAV-SfM Approach." *Earth Surface Processes and Landforms* 42 (9): 1434–43. https://doi.org/10.1002/esp.4139.

Acknowledgements

This research was supported by the company Electricité de France (EDF) within the research collaboration 'Redynamization of the Old Rhine – years 2014-2018' (EDF 5910132058). The Teledyne Optech Titan DW lidar sensor used in this study is operated by the Nantes-Rennes Topo-Bathymetric lidar platform (University of Rennes 1/University of Nantes). The authors thank Patrice Carbonneau for helpful recommendations and Pierre-Alexis Herrault for the computation of metrics characterizing the point clouds.

948

949